Exp Fluids (2017) 58:18
DOI 10.1007/s00348-017-2305-2

RESEARCH ARTICLE

A comprehensive statistical investigation of schlieren image velocimetry (SIV) using high-velocity helium jet

Sayan Biswas[1] · **Li Qiao**[1]

Received: 10 June 2016 / Revised: 4 January 2017 / Accepted: 19 January 2017

Abstract A detailed statistical assessment of seedless velocity measurement using Schlieren Image Velocimetry (SIV) was explored using open source Robust Phase Correlation (RPC) algorithm. A well-known flow field, an axisymmetric turbulent helium jet, was analyzed near and intermediate region ($0 \leq x/d \leq 20$) for two different Reynolds numbers, $Re_d = 11{,}000$ and $Re_d = 22{,}000$ using schlieren with horizontal knife-edge, schlieren with vertical knife-edge and shadowgraph technique, and the resulted velocity fields from SIV techniques were compared to traditional Particle Image Velocimetry (PIV) measurements. A novel, inexpensive, easy to setup two-camera SIV technique had been demonstrated to measure high-velocity turbulent jet, with jet exit velocities 304 m/s (Mach = 0.3) and 611 m/s (Mach = 0.6), respectively. Several image restoration and enhancement techniques were tested to improve signal to noise ratio (SNR) in schlieren and shadowgraph images. Processing and post-processing parameters for SIV techniques were examined in detail. A quantitative comparison between self-seeded SIV techniques and traditional PIV had been made using correlation statistics. While the resulted flow field from schlieren with horizontal knife-edge and shadowgraph showed excellent agreement with PIV measurements, schlieren with vertical knife-edge performed poorly. The performance of spatial cross-correlations at different jet locations using SIV techniques and PIV was evaluated. Turbulence quantities like turbulence intensity, mean velocity fields, Reynolds shear stress influenced spatial correlations and correlation plane SNR heavily. Several performance metrics such as primary peak ratio (PPR), peak to correlation energy (PCE), the probability distribution of signal and noise were used to compare capability and potential of different SIV techniques.

Abbreviations

BOS	Background-oriented schlieren
CWO	Continuous window offset
PCE	Peak to correlation energy
PDF	Probability distribution function
PIV	Particle image velocimetry
PPR	Primary peak ratio
RMS	Root mean square
ROI	Region of interest
RPC	Robust phase correlation
SIV	Schlieren image velocimetry
SNR	Signal to noise ratio
UOD	Universal outlier detector
d	Nozzle diameter
d_p	Particle image size, pixel
D_p	Tracer particle diameter in PIV
i	Intensity
n_p	Number of particles in interrogation window
Re_d	Reynolds number
U_0	Centerline jet velocity
x, r	Jet coordinate
N	Sample size

1 Introduction

Particle image velocimetry (PIV) is a quantitative optical method used in experimental fluid dynamics that captures entire 2D/3D velocity field by measuring the displacements of numerous small particles that follow the motion of the

✉ Sayan Biswas
biswas5@purdue.edu

[1] School of Aeronautics and Astronautics Engineering, Purdue University, West Lafayette, IN 47906, USA

Published online: 17 February 2017

fluid. In its simplest form, PIV acquires two consecutive images (with a very small time delay) of flow field seeded by these tracer particles, and the particle images are then cross-correlated to yield the instantaneous fluid velocity field. Nature of PIV measurement is rather indirect as it determines the particle velocity instead of the fluid velocity. It is assumed in PIV that tracer particles "faithfully" follow the flow field without changing the flow dynamics. To achieve this, the particle response time should be faster than the smallest time scale in the flow. The flow tracer fidelity in PIV is characterized using Stokes number, S_k where a smaller Stokes number $\left(S_k < 0.1\right)$ represents excellent tracking accuracy. Conversely, schlieren and shadowgraph are truly non-intrusive techniques which rely on the fact that the change in the refractive index causes light to deviate due to optical inhomogeneities present in the medium. Schlieren methods can be used for a broad range of high-speed turbulent flows containing refractive index gradients in the form of identifiable and distinguishable flow structures. In schlieren image velocimetry (SIV) techniques, the eddies in a turbulent flow field serve as PIV "particles". Unlike PIV, there are no seeding particles in SIV. To avoid confusion, a quotation mark is used for "particles" when describing the SIV techniques. As the eddy length scale decreases with the increasing Reynolds number, the length scales of the turbulent eddies become exceptionally important. These self-seeded successive schlieren images with a small time delay between them can be correlated to find velocity field information. Thus, the analysis of schlieren and shadowgraph images is of great importance in the field of fluid mechanics since this system enables the visualization and flow field calculation of unseeded flow.

Papamoschou (1989) showed the possibility of using schlieren technique to measure the velocity of very high-velocity flows. A schlieren system with a pulsed light source and a very short (~20 ns) camera exposure time was utilized to measure a supersonic shear layer. However, due to the lack of processing power, only a global convective velocity of the turbulent shear layer was captured using pattern matching technique between two consecutive schlieren images. (Fu and Wu 2001; Li et al. 2009; Fu et al. 2000) was among the first to use high-speed (~100 kHz) imaging to extract velocity field from sequences of schlieren images. All previous works used application-specific image processing algorithm, until the substantial development of digital PIV (DPIV) towards the end of the twentieth century, when the digital PIV processing algorithm was commonly and commercially available.

Elsinga et al. (2003, 2004); Raffel et al. (2000a, b); Raffel (2015); Scarano et al. (1999) computed flow field information using background-oriented schlieren (BOS) technique using the evaluation algorithms proposed by Rafael and Goldhahn (Kindler et al. 2007; Goldhahn and Seume 2007). Kegerise and Settles performed image correlation velocimetry on an axisymmetric turbulent-free convection plume (Kegerise and Settles 2000). Garg and Settles performed turbulence measurements of the supersonic turbulent boundary layer by focusing schlieren deflectometry technique (Garg and Settles 1998). Jonassen and Settles (2006) explored the possibility of using commercial PIV equipment combined with schlieren optics to measure the velocity field of an axisymmetric helium jet and a 2D supersonic turbulent boundary layer. A laminar jet structure at the exit prevented them from capturing the tip and near-field velocities of helium jet. However, Jonassen compared different schlieren and shadowgraph sensitivity settings to find an optimum sensitivity value. Later, (Hargather et al. 2011; Hargather and Settles 2012) compared three quantitative schlieren techniques, Schardin's calibrated schlieren, rainbow schlieren and background-oriented schlieren (BOS) using a 2D turbulent boundary layer. Most recently, Mauger et al. (2014) performed velocity measurements in a cavitating microchannel two-phase flow configuration using shadowgraph image correlations. Zelenak et al. (2015) conducted an experiment to test the applicability of the laser shadowgraph technique combined with commercial PIV processing algorithms to visualize the pulsating water jet structure and to analyze the velocity field.

All the aforementioned schlieren or schlieren-like velocimetry techniques used either application specific, home-grown image processing algorithms or commercial digital PIV software to obtain flow field information. Since commercial PIV software had been developed keeping digital PIV in mind, processing parameters are not optimized for SIV. Until now all studies on schlieren velocimetry techniques were accentuated how well SIV techniques agree compared to a well-established velocity measurement technique such as hot wire, LDV or PIV. No such detailed study was conducted on the performance of different image correlation algorithms and the effect of various preprocessing and post-processing techniques for SIV. Additionally, very few past studies used SIV to resolve high Reynolds number flows except Hargather's work (Hargather et al. 2011) in which the mean velocity profile of a Mach 3 turbulent boundary layer was measured. The challenge for high-speed flows lies in the fact that SIV requires extremely expensive digital cameras—either a very high-speed camera (100 kHz or up) or a multi-exposure camera is needed to resolve a high-speed velocity field using SIV.

Motivated by this, the present study provides a comprehensive statistical assessment of three different SIV techniques, schlieren with horizontal knife-edge cutoff, schlieren with vertical knife-edge cutoff and shadowgraph, for a high velocity ($0.3 < \text{Mach} < 0.6$) helium jet using an open source robust phase correlation (RPC) (Eckstein and Vlachos 2009) code. RPC shows enhanced

measurement capabilities regarding better signal to noise (SNR) ratio, reduction of bias error and peak locking. This paper is one of the very first to apply SIV techniques to measuring high-speed flows. Experimental measurement of high-speed flows is extremely challenging. At high speeds, the chances that PIV tracer particles will not "faithfully" follow the flow increase. Thus, it becomes increasingly difficult to apply PIV to high-speed flows. Since SIV techniques do not require seeding particles, they provide an alternate solution. However, to date very few studies measured velocities of high-speed flows using SIV techniques due to two reasons. The first reason is hardware limitations of the camera and the second is due to the absence of a well-established post-processing routine. In the present paper, we proposed a novel, inexpensive two-camera approach to solving this problem. Using two high-speed cameras side by side to capture schlieren images effectively forms a double-exposure high-speed camera. This two-camera approach has never been explored and can be very helpful to resolve high-speed axisymmetric or 2D flows. A highly resolved temporal and spatial velocity field was obtained using two cameras in parallel. Unlike PIV, image pre-processing, conditioning, filtering, image processing and post-processing are all different for SIV. Optimization of SIV processing parameters, various types of image filtering, image restoration and noise reduction techniques useful for SIV techniques were discussed in detail. Because the ratio of the time-scales of the smallest and largest eddies (τ_η and τ_0) varies with Reynolds number, $\tau_\eta/\tau_0 \sim \mathrm{Re}^{-1/2}$ (Pope 2000), the size ratio of the biggest and smallest windows in SIV methods also depends on the Reynold number. Although previous studies compared their SIV results to PIV, LDV or hot wire measurements, none statistically explained the performance of SIV. A comprehensive analysis of different SIV techniques was carried out using the correlation planes statistics. Correlation plane statistics for various SIV techniques depended primarily on turbulence parameters such as turbulence intensity. Quantitative comparison of correlation planes at different spatial locations of high-speed axisymmetric helium jet was performed. Several performance metrics such as primary peak ratio (PPR), peak to correlation energy (PCE), and the probability distribution of SNR were used to compare capabilities of different SIV techniques. This paper combined an open source PIV processing algorithm with a novel two-camera, easy to setup SIV technique with a detailed description of image preprocessing, flow field post-processing, and their statistical assessment, therefore, presented a solution to resolve velocity fields of a wide range of turbulent flows.

2 Experimental method

The experimental setup is schematically shown in Fig. 1a. A steady helium jet was issued from a nozzle at velocity U_0 into a quiescent ambient. The nozzle had a diameter of 4 mm and a length to diameter ratio, L/d, of 2. Schematic of the axisymmetric jet coordinates (x, r) is shown in Fig. 1b. The jet centerline velocity, $U_0(x)$ decayed as the jet spread, $\delta(x)$ in the streamwise direction. The upstream nozzle pressure was carefully controlled using Kulite (XTEL-190) pressure transducers combined with NI-9237 signal conditioning module to create two different flow conditions at the nozzle exit: $Re_d = 11{,}000$ and $Re_d = 22{,}000$, respectively. The jet Reynolds number, Re_d, is defined as, $\mathrm{Re}_d = U_0 d/\nu$, where U_0 is the jet exit velocity, d is the nozzle diameter, and ν is the kinematic viscosity at the nozzle exit. For Reynolds number 11,000 and 22,000, the jet centerline velocity at the nozzle exit was 304 m/s (Mach = 0.3) and 611 m/s (Mach = 0.6), respectively, based on the PIV measurements. The theoretical jet exit velocity calculated from experimentally measured pressure drop across the nozzle using plug flow assumptions was 297 and 601 m/s, respectively, which agreed well with the PIV data.

2.1 High-speed schlieren and shadowgraph imaging

A z-type Herschellian high-speed schlieren system was used to visualize the axisymmetric turbulent helium jet. The schlieren system consisted of a 100 W mercury arc lamp (Q series, 60064-100MC-Q1, Newport Corporation, Model 6281) light source with a condensing lens assembly (Q Series, F/1, Fused Silica, Collimated, 200–2500 nm), two concave parabolic mirrors (6″ diameter, aperture f/8, effective focal length 1219.2 mm), a knife-edge, an achromatic lens ($f = 300$ mm) to collimate the light, a beam splitter (1″ cube, Thorlabs PBS251) and two identical high-speed CCD cameras (Phantom v711, Vision Research). The inter-frame delay, Δt, between the two high-speed cameras was accurately controlled by a low jitter digital delay generator (Stanford Research, DG535). The inter-frame delay needed to be small enough to resolve high jet velocity. The same setup as shown in Fig. 1a was used for shadowgraph with minor modifications. No knife-edge was used as shadowgraph does not require any cutoff of refracted light.

The jet velocity at the nozzle exit U_0 was within the range of 300–600 m/s ($0.3 < \mathrm{Mach} < 0.6$) and the length scale of the turbulent structures within the jet was typically in the order of millimeters. To capture such flow details and to extract a meaningful correlation between consecutive images, an extremely high framing rate was required. For example, to observe a 10×10 cm^2 ROI in a flow field flowing at a velocity of 500 m/s, it requires a minimum 80 kHz frame rate for an optimum 10–12 pixels shift between

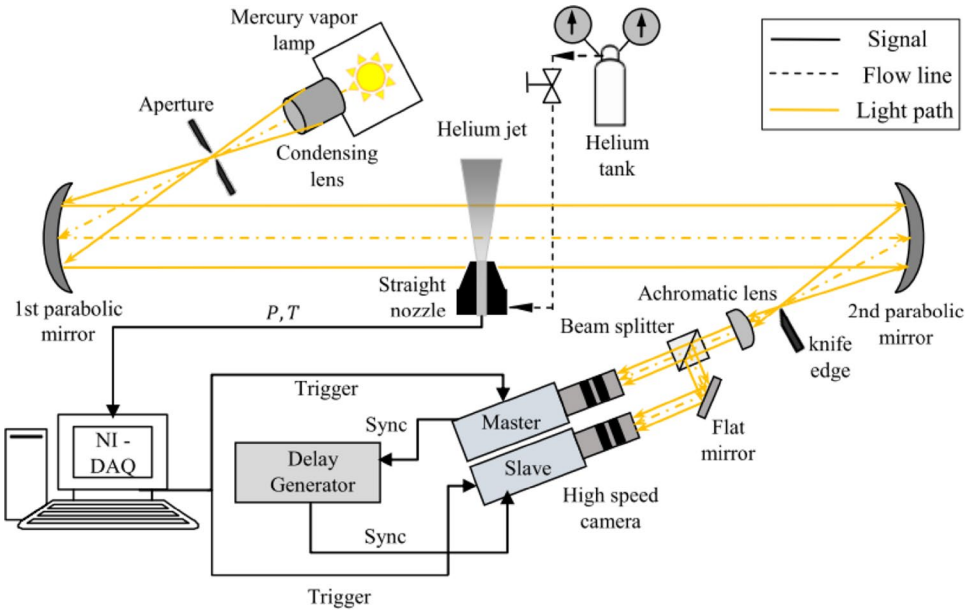

(a)

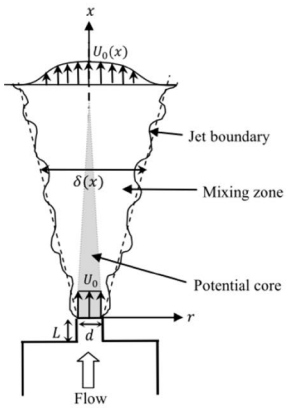

(b)

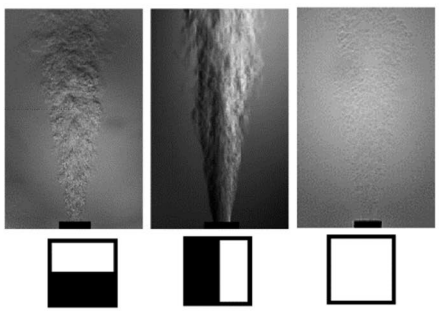

(c)

Fig. 1 Schematic of **a** an experimental setup for high-speed schlieren imaging of axisymmetric helium jet, **b** a free jet issuing from a straight nozzle and its coordinate system, **c** schlieren photographs of turbulent helium jet using a horizontal knife-edge (*left*), vertical knife-edge (*right*), and shadowgraph

consecutive images with a 1000×1000 pixels camera resolution. Moreover, to reduce integration effect, camera exposure time should be less than frame-to-frame time delay, Δt. To solve this problem, two identical black and white Phantom high-speed digital cameras with an identical lens system (105 mm Nikon f/2.8G macro lens) were used to capture schlieren visualization, with a time delay, Δt, in between the two cameras (master and slave). This time delay, Δt, was precisely controlled by the delay generator DG535 and could go as small as 0.1 μs. For $Re_d = 11{,}000$ and $Re_d = 22{,}000$ the time delay, Δt between the two cameras were set 0.4 and 0.2 μs, respectively. Both cameras were synchronized with a master trigger to start the recording. Each frame of the slave camera was synchronized with the corresponding frame of the master camera by the time delay Δt. Schlieren images were captured with a resolution of 1024×800 pixels with a framing rate up to 10,000 frames per second. As for the spatial resolution, the size of the evaluated area was 84×64 mm^2. Using two high-speed cameras side by side to capture schlieren images was an effective way to form a double exposure high-speed camera. During image processing, each frame from the master camera was correlated with the corresponding frame from slave camera. Thus, corresponding image pairs from master and slave cameras were correlated. So, the user-defined time delay, Δt,was the delay between these two images. The framing rate for both cameras was identical, and it merely dictated the number of image pairs acquired over a period.

Figure 1c describes the orientation of the knife-edge for schlieren. For both the knife-edge orientations, 40% cutoff of refracted light was used since 40% was the optimum cut-off that provided the best SNR. The contrast of the schlieren

images would had increased with the higher percentage of light cutoff, but that would have had also decreased "particle" image size. This is discussed in detail in the data preprocessing section. In Fig. 1c, the helium jet on the left represents horizontal knife-edge. It detected changes only in the vertical component of the refractive index, $\partial n/\partial x$ of the jet. The middle image of the helium jet shows the result using a vertical knife-edge where only changes in the horizontal component of the refraction index, $\partial n/\partial r$, were detected. Shadowgraph, the right most image of Fig. 1c, did not require knife-edge.

It was essential to characterize the shadowgraph and schlieren system. Shadowgraph intensity is defined as the ratio g/h, where g is the focus offset between schlieren and the focal plane and h is the distance between the collimating lens/mirror and the focal plane (Settles 2001). A g/h value of 0.31 was used for shadowgraphy. The schlieren sensitivity or the contrast sensitivity can be written as the rate of change of image contrast with respect to refraction angle, $\mathbb{S} = d\mathbb{C}/d\epsilon$. Contrast, $\mathbb{C}$ in the schlieren images can be expressed as the ratio of differential luminance, ΔE to the general background level, E. $\mathbb{C} = \Delta E/E = \Delta a/a$, where a is the unobstructed height of the source image in the cutoff plane, and Δa represents the change in a due to refraction. The refraction angle is ϵ. The schlieren sensitivity can be further simplified to $\mathbb{S} = f_2/a$, where f_2 is the focal length of the second parabolic mirror. This simple yet sufficient geometric-optical relation for sensitivity adequately characterizes the schlieren system. For both schlieren settings (horizontal knife-edge and vertical knife-edge), $f_2 \cong 1.2$ m and $a \cong 500$ μm produced a schlieren sensitivity, $\mathbb{S}$ of 2400.

2.2 PIV imaging

To validate the flow field results from SIV techniques, traditional 2D PIV was carried out on this axisymmetric helium jet under identical experimental conditions. A double oscillator 532 nm Nd:YAG laser was used, which delivers an energy of 50 mJ per pulse with a pulse duration of 6 ns and at a sampling frequency of 15 Hz. The laser beam was converted into a laser sheet of 1 mm thickness. The jet was seeded with titanium dioxide (TiO_2) tracer particles with a nominal diameter, D_P of 0.4 μm. Particle Stokes number, S_k, was 0.035 and 0.07 for $Re_d = 11{,}000$ and $Re_d = 22{,}000$, respectively. A digital CCD camera from TSI Inc. (4MP-HS) with a 105 mm Nikon f/2.8G microlens was used to capture a field of view (FOV) of approximately 84.5×64.5 mm^2. Multiple sets of 500 images were taken for each Reynolds number. PIV data acquisition was made using the TSI Inc. software. Since PIV and SIV were executed on identical experimental settings, the same PIV camera could have been used for schlieren measurements as well. However, the intention of SIV was to get a highly time-resolved measurement of the steady helium jet (and ultimately for other unsteady, transient jets), which is why two high-speed cameras were used for schlieren and shadowgraph measurements. Two high-speed cameras side by side, each at 10,000 frames per second, effectively created a double exposure 10 kHz system. This was not possible with the PIV camera which was a double exposure 32 fps maximum with a pixel resolution of 2048×2048 pixels, even after sacrificing some of its spatial resolutions.

2.3 Calibration

The standard PIV calibration approach was applied to SIV as well. A planar target with a regularly spaced (0.5 mm) grid of markers was placed on the light path at the position of the schlieren object (the helium jet). It was moved by a specified distance in the out-of-plane direction to two or more positions to ensure alignment and to minimize any distortion in the two-camera system. At each position, a calibration polynomial mapping function with sufficient degrees of freedom mapped the global x–r plane to camera planes.

3 Data analysis techniques

Data analysis procedures are composed of three major segments. Data pre-processing techniques including image filtering, inverse Abel transform, and particle size limitations are discussed in first part, followed by data processing parameters such as correlation algorithm, grid size, window size, overlapping parameter, etc. The final section discusses post-processing methods.

3.1 Data preprocessing parameters

3.1.1 "Particle" image size and "Particle" density

In PIV, two critical parameters that control bias and root-mean-square (RMS) error are particle image size, d_p, the size of the particle image in pixels and particle density, n_p, the number of particle images per interrogation window. A particle image size less than 1 pixel creates peak locking and higher than 3 pixels brings bias error (Fincham and Spedding 1997). Likewise, a lower particle density, $n_p < 8$ incurs mean bias and root-mean-square (RMS) error. To minimize errors in PIV, researchers have found a particle image size in the range of $2 < d_p < 3$pixels and a particle density in the range of $8 < n_p < 22$ work best for cross-correlation-based PIV processing algorithms (Huang et al. 1997). In PIV experiment, this particle image size is meticulously controlled by the projected pixel resolution factor (μm/pixels) during the calibration process.

An edge detection method was implemented in SIV to ensure the minimum "particle" density requirement. Marr and Hildreth (1980) edge detection algorithm that combines Gaussian filtering with the Laplacian was used to detect "particle" edges. A typical SIV "particles" map is shown in Fig. 2 using Marr and Hildreth edge detection method. Two different interrogation windows, 'window A' (rectangular) and 'window B' (square), are shown on this "particles" map. A quick overview to generate a "particles" map using Marr and Hildreth algorithm is outlined here. First, a Gaussian filter was applied to the entire image. Then, zero crossings were detected in the filtered image to obtain the edges. Zero-crossing occurs when the brightness changes over a threshold gray scale value. This threshold gray value is user-defined, and we used the average gray value of the respective images. Marr and Hildreth edge detection method is particularly suitable when there are substantial and rapid variations in image brightness. Although Canny edge detection method (Canny 1986) generally does a better job in detecting edges, the edge contours can be substantially fragmented. On the contrary, Marr and Hildreth edge detection algorithm always forms connected closed contours that help easy detection of SIV "particles".

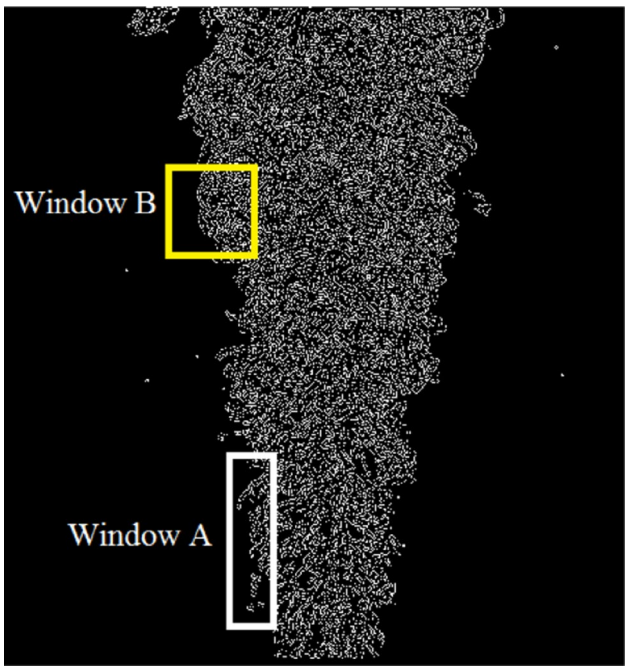

Fig. 2 Typical SIV "particles" using Marr and Hildreth edge detection method

However, in SIV techniques, there are no real particles. Rather turbulent eddies are considered as seeding "particles". Since we were using an open source processing code designed for PIV, we chose to follow these error minimizing guidelines for SIV techniques as well. Figure 3 shows the "particle" image size, d_p for schlieren and PIV, respectively. For both cases, the intensity-weighted "particle" image size lied within the range of $2.6 < d_p < 2.9$ pixels. However, the eddy size changes with the change in integral length scale along the axial direction of the jet. Figure 4 shows the variation of "particle" image sizes, d_p along the jet in SIV. "Particle" size increases in a monotonic fashion from $d_p = 1.7$ pixels at the jet exit to $d_p = 3.2$ pixels at $x/d = 20$. Nevertheless, "particle" sizes fall in the range of $2 < d_p < 3$ pixelsfor most of the near and intermediate regions, $4 < x/d < 16$. This was achieved by precisely controlling the projected pixel resolution factor in SIV measurements. A projected pixel resolution of 80 μm/pixel was used for the current experiment.

"Particle" density, n_p, dictates the window sizes during post-processing, for both PIV and SIV techniques. Window sizes for multiple passes were chosen carefully to reduce

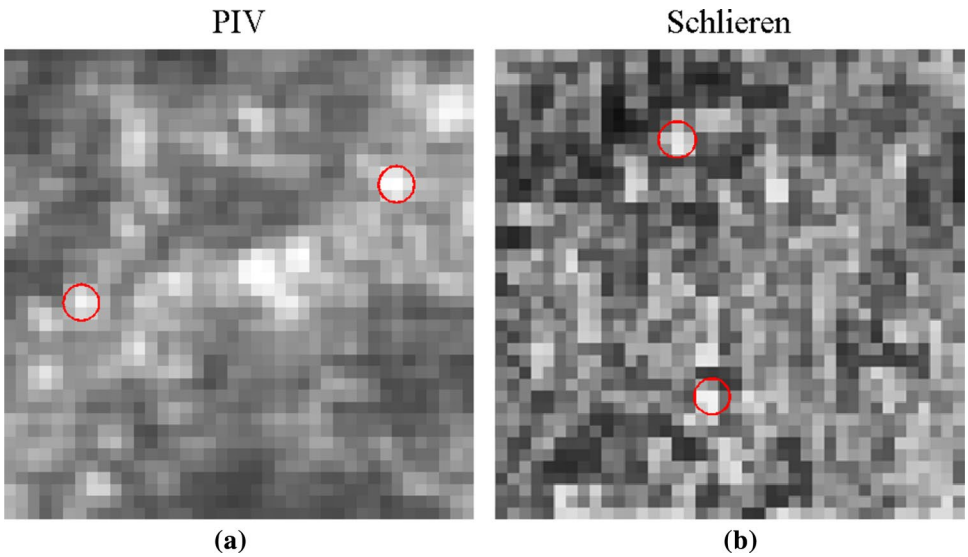

Fig. 3 Unfiltered 40×40 pixels image segments from **a** PIV and **b** schlieren showing particle image size, d_p (approximately marked by a *red circle*). The "particle" image size lies between, $2 < d_p < 3$ pixels

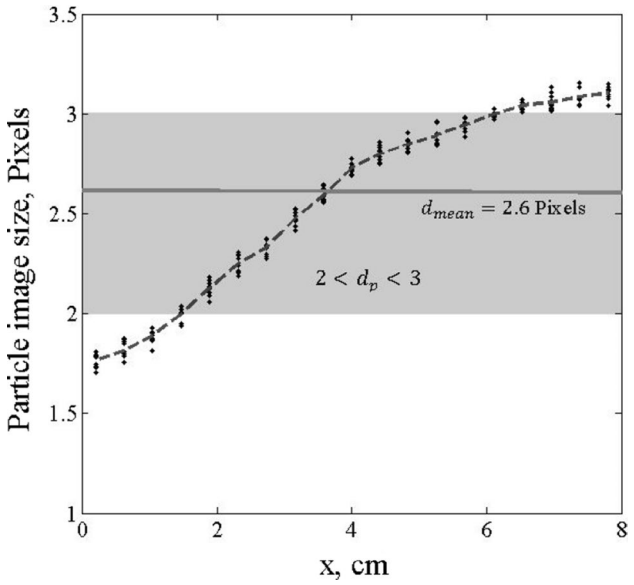

Fig. 4 Variation of "particle" image size, d_p along the jet in SIV techniques

errors. The first pass was dictated by the maximum velocity of the flow field. In other words, the largest window size was required in the first pass to resolve the highest velocity. This window size automatically included enough "particles". However, for the successive passes, the window size was reduced in a manner so that the interrogation window held just enough "particles", n_p to reduce the bias error. Window sizes of 32×128 pixels and 16×16 pixels were selected for the first pass and the final pass, respectively.

3.1.2 Inverse Abel transformation

Contrary to 2D PIV where the probe volume is made of a laser sheet with a thickness of 1 mm or less, schlieren and shadowgraph produce path integrated volumetric signals. Thus, a reverse Abel transform (Jonassen et al. 2006; Abel 1826; Arfken et al. 2012) was necessary. For an axisymmetric jet, the local intensity i can be evaluated using the inverse Abel transformation of the line of sight intensity, I which is obtained from the intensity measurement as a result of change in refractive index from schlieren images. The relationship between the local intensity, i and the line of sight intensity, I under axisymmetric assumption can be expressed as:

$$i = -\frac{1}{\pi}\int_r^\infty \frac{\mathrm{d}I}{\mathrm{d}y}\frac{\mathrm{d}y}{\sqrt{y^2 - r^2}} \tag{1}$$

where r is the radial distance as shown in Fig. 1b, and Zy is the distance from the jet centerline perpendicular to the line of sight direction. Then, the local intensity i can be calculated using Eq. 1. Figure 5a shows the Abel inversion of a typical schlieren image of the turbulent round jet. Figure 5b compares the line intensity at an axial location $z = 200$ pixels before and after the Abel inversion.

Abel transformation requires an axial symmetry of the velocity field. The temporally and spatially averaged mean flow field fulfilled this assumption. However, the instantaneous flow field extracted from the consecutive schlieren images did not fulfill this assumption of symmetry. Thus, to apply Abel inversion on instantaneous schlieren images, it was essential to study the behavior of time averaged Abel inversion under varying sample size i.e., the number of SIV images. As shown in Fig. 5 that for a 2D intensity map of schlieren images, Abel inversion affected the intensity values of the jet. However, at times numerical error could propagate while solving the inverse Abel transform equation. Thus, an ensemble time averaging of a set of five, ten and 50 schlieren images for each test condition was compared to examine the noise in the Abel inversion

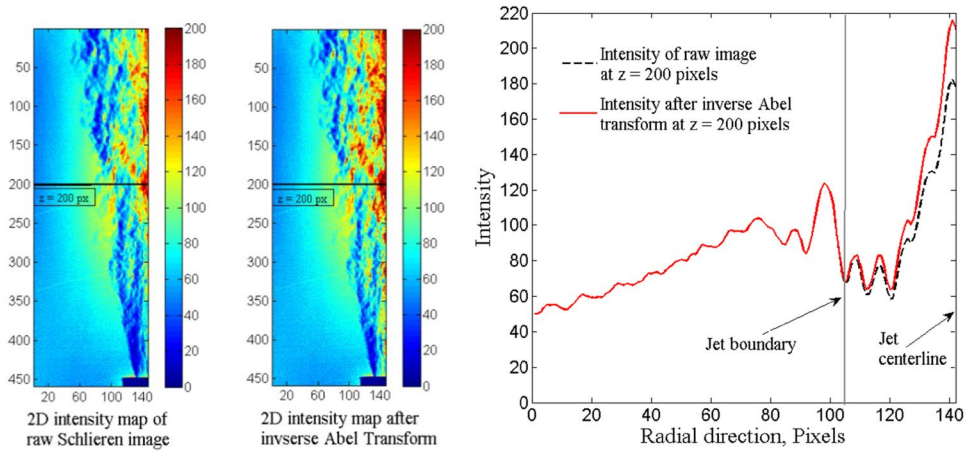

Fig. 5 The effect of Abel inversion on **a** a typical schlieren image of the turbulent round jet, and **b** the line intensity at an axial location of $z = 200$ pixels

and is shown in Fig. 6. We studied the variation of the Abel transformed quantity (image intensity) for three different sample sizes, $N=5$, 10 and 50. As we increased the number of images to $N=50$, the inversion attained a mean value. However, as we decreased the sample size to $N=5$, nominal scatter was observed around the mean, but overall the variation was relatively small as evident from Fig. 6. Since the Abel inversion only negates the effect of volumetric path integration nature of schlieren images, once we achieved a steady inversion, unless we changed the experimental conditions such as light intensity, knife-edge cutoff, camera settings, the variation in Abel transformed quantity (image intensity) was negligible. Previous studies (Coppalle and Joyeux 1994; Mayrhofer and Woisetschläger 2001; Yildirim and Agrawal 2005; Joshi and Schreiber 2006) showed the potential of using Abel inversion to transform an instantaneous axisymmetric measurement into the planar measurement.

3.1.3 Image filtering

Image restoration and enhancement play a significant role in both traditional PIV as well as for SIV techniques. Traditional PIV has proven preconditioning techniques to attenuate or completely remove undesired effects via image reconstruction (e.g., background subtraction) or image enhancement (e.g., min–max contrast normalization). Since the physical processes behind schlieren and shadowgraph techniques are completely different than PIV, not all image reconditioning methods commonly used for PIV can be implemented on schlieren images. A variety of image filtering techniques were tested, and some of them are discussed in the following.

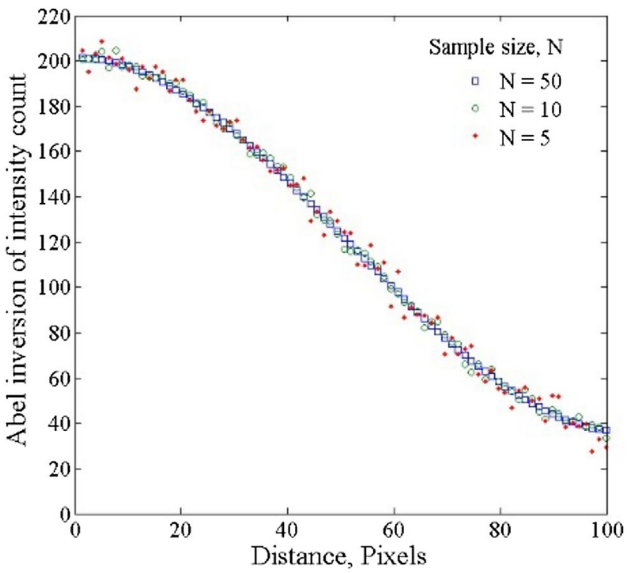

Fig. 6 Abel inversion of schlieren intensity counts for different sample sizes

The quality of the present PIV images suffered due to pulse to pulse variation of the light intensity from the Nd:YAG laser. Intensity normalization fixed this issue. PIV images also contained dark current and thermal noise of a CCD sensor. Due to homogeneous statistical properties of this noise, a background subtraction greatly reduced it. Background subtraction also reduced the effects of laser flare and other stationary image features. Lastly, to smooth out small-scale intensity fluctuations a uniform filter, which is a linear low-pass filter, was used to replace each pixel by the average gray value over a 3×3 pixels subdomain. After applying the uniform filter, the resulting image was subtracted from the original image. Resulted improvements are shown in Fig. 7a along with the gray value histograms for a PIV image segment. The left image of Fig. 7a shows a noisy PIV image segment with random noise fluctuations as evident from the widely distributed gray value histogram. After an intensity normalization, background subtraction, and uniform filtering, the gray value histogram reduced in width, as shown in the right side of Fig. 7a. Similar image improvements were obtained using a Gaussian filter instead of the uniform filter as well.

PIV image intensity field involved bright particle images on a darker background, whereas the schlieren and shadowgraph images contained turbulent structures on a gray color background. It was impossible to use background subtraction on schlieren images without removing some of the actual signals. That is why image enhancement or amplification served best rather than image reconstruction for SIV techniques. For all SIV images, first, a narrow-width, low-pass filter was applied to remove high-frequency noises (e.g., camera shot noise, pixel anomalies, and digitization artifacts) from the images. This also allowed the sub-pixel peak fitting algorithm to perform better by widening the correlation peaks. Contrast enhancement increased signal content in SIV images and helped to find the definite correlation between successive images. In other words, optimization of image contrast was necessary for SIV. A nonlinear min/max filter approach as suggested by Westerweel (1993) was used to normalize the image contrast. Lastly, to enhance the edges of the turbulent structures, Laplace filter (Rosenfeld and Kak 1982) was applied. Due to the highest velocity near the jet tip, there was always a chance that a longer camera exposure time could blur turbulent structures and could create an under-sampled image segment. This could lead to the so-called peak-locking effect. However, a high-pass Laplace filter reduced this adverse effect. The combined effects of all these filters are shown in Fig. 7b–d for schlieren with a horizontal knife-edge, schlieren with vertical knife-edge and shadowgraph, respectively. Gray value histograms behave fairly similarly for schlieren with

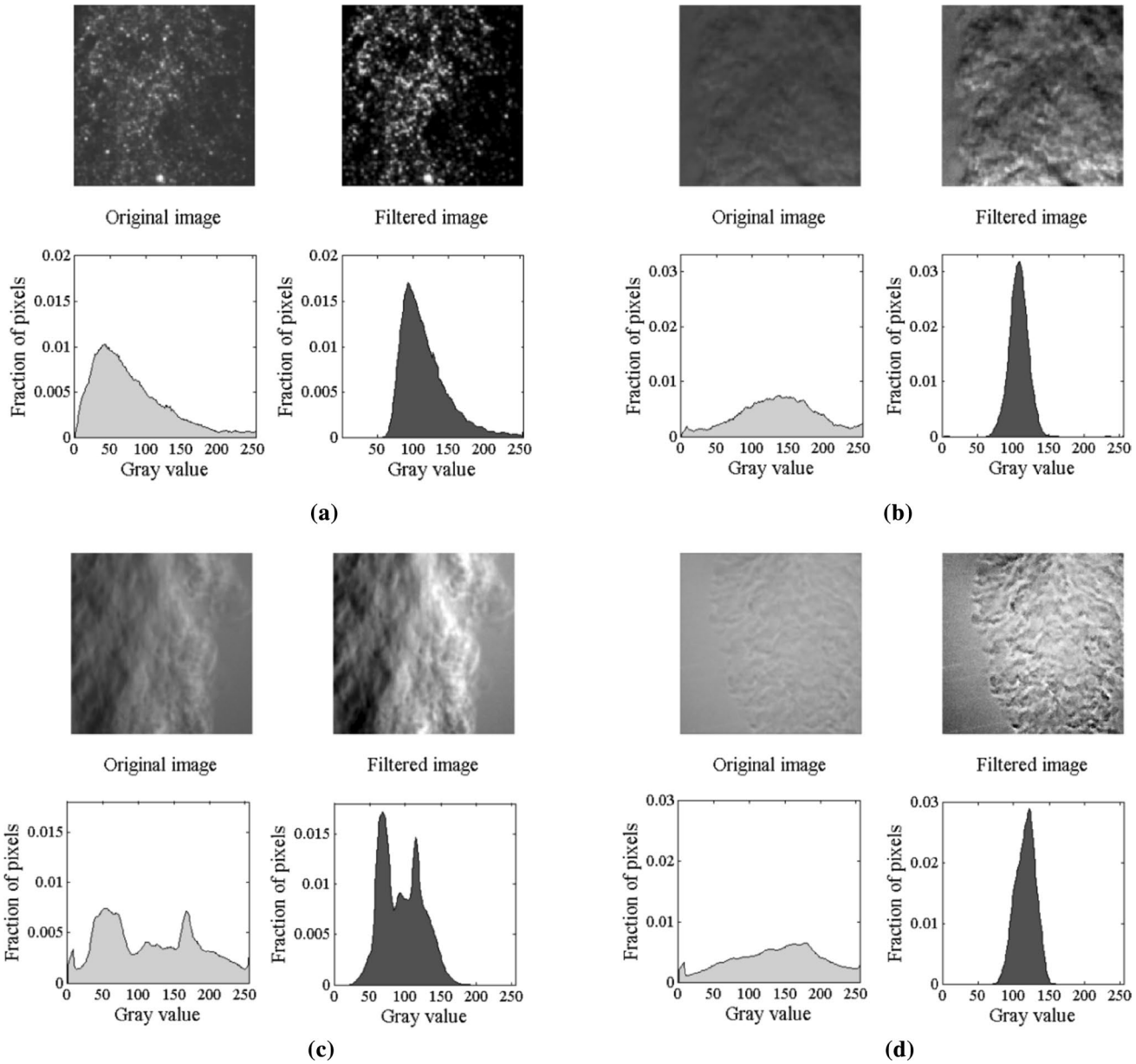

Fig. 7 Improvement of image segmentation and gray value histograms for **a** PIV, **b** schlieren with horizontal knife-edge, **c** schlieren with vertical knife-edge, and **d** shadowgraph

horizontal cutoff and shadowgraph as gray levels narrow down between 60 and 150 for filtered images compared to their original counterparts spreading across entire 0–255 Gy value range.

While the gray value histograms of filtered image segments for schlieren with horizontal knife-edge and shadowgraph demonstrated improvements over the original image, schlieren with vertical knife-edge failed to do so. Vertical knife-edge produced an uneven illumination on left and right sides of the schlieren image as shown in Fig. 1c. Thus, double-peaked gray value histogram appeared as depicted in Fig. 7c. Even with this limitation, vertical knife-edge schlieren was investigated in this paper for the comparison purposes between different SIV techniques.

For white-light schlieren, the darkness of the gray background increased with increase in knife-edge cutoff. An increasing cutoff also enhanced image contrast. However, this increase in the contrast came at the cost of lower "particle" size with higher cutoff (Jonassen et al. 2006). This was the prime reason why 40% cutoff for both the horizontal and vertical knife-edge schlieren was chosen in the first place.

3.2 Data processing parameters

The data were post-processed using an open source GUI-driven Matlab code, quantitative imaging (QI) or Prana (35) originally developed at the AEThER Laboratory of Virginia Tech. Robust phase correlation (RPC) (Eckstein and Vlachos 2009) algorithm was used, which essentially uses the phase of the Fourier transform-based cross-correlation plane and applies a Gaussian spectral filter to optimize the SNR. The use of RPC algorithm becomes justified from Fig. 3b that showed the intensity distribution of turbulent structures from schlieren images. Intensity map of turbulent eddies in schlieren images looked approximately Gaussian. A higher order multi-grid continuous window offset (CWO) iterative image deformation method was applied throughout, for which the image window was deformed to diminish the loss of information due to shear and/or rotation of the image windows. Additionally, bicubic interpolation for velocity field interpolation and the cardinal function with Blackman filter for image interpolation were employed. To obtain a converged velocity field, a total of 4–5 iterations with varying processing parameters such as grid size, window size, resolution, and vector validation were used. To resolve higher velocities at the jet exit, a rectangular window of 1:4 ratio (32×128 pixels, 16×64 pixels) where the long side of the window aligned streamwise (or in the x direction) was used on the first pass. This generated 50% overlap in the radial direction and 87.5% overlap in the streamwise direction. A 1:1 16×16 pixels interrogation window size with 50% overlap at the final pass was applied, leading to a vector spacing of 0.4 mm for the time-resolved measurements. Grid resolution of 8×8 pixels and a particle image diameter of 2.8 pixels were used. The three-point Gaussian estimator was employed for the subpixel correlation peak location for interpolating the correlation peak location (and hence displacement) below the specified pixel resolution.

3.3 Data post-processing parameters

3.3.1 Validation of velocity field

Post-processing parameters were set up separately for each pass for all measurement techniques. Two essential validation techniques, velocity thresholding and universal outlier detection (UOD), were implemented to obtain the final velocity field for all passes except the final pass. To remove high-frequency noise signals, a Gaussian smoothing filter was applied to each vector field by taking an average value of the neighborhood grid points.

4 Results and discussion

The velocity fields of the helium jet obtained from PIV and SIV techniques are discussed in Sect. 4.1. Section 4.2 compares the spatial variation of correlation planes from different SIV methods with PIV. Lastly, a statistical survey of different methods is conducted in Sect. 4.3.

4.1 Helium jet results

An Abel inversion was applied during SIV data processing to find the true velocity field. Figure 8a shows that an Abel inversion was necessary for the SIV to yield comparable results to the PIV data. The effect of Abel inversion is maximum at the jet centerline, $r = 0$ since the effect of path integration reaches highest at the centerline. The Abel inversion was applied on schlieren images in the beginning of the data processing, even before applying any image enhancement/restoration technique. Several past studies (Jonassen et al. 2006; Watt et al. 2000) performed this step, an inverse Abel transform, during the post-processing of SIV data. Thus, we wanted to understand and validate the effect of Abel inversion at two different stages

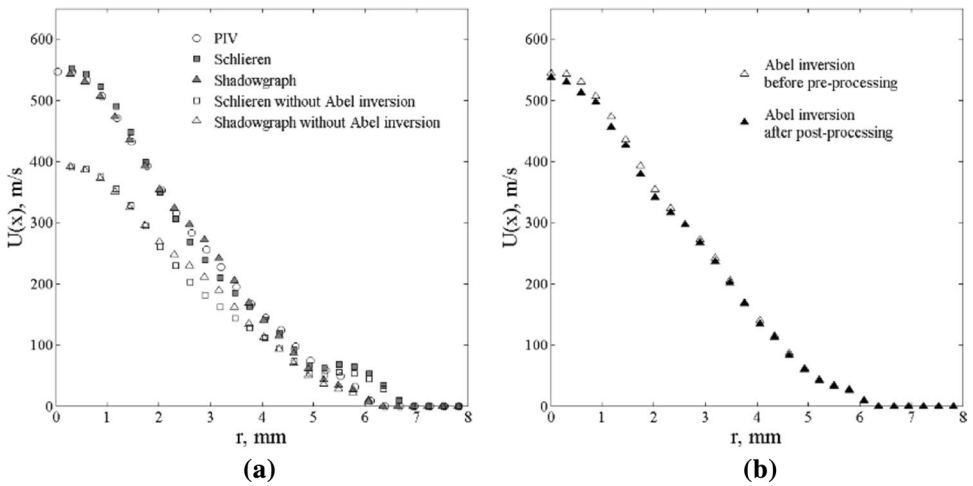

Fig. 8 **a** Comparison of SIV results with PIV before and after Abel inversion, **b** Abel inversion at different stages of data processing for $x/d = 10$ of $Re_d = 22{,}000$ jet

of data processing, (1) at the beginning of the pre-processing, before applying image filters, (2) after the processing (cross-correlation) and data validation, at the very last step. Figure 8b compares Abel inversion of a schlieren velocity profile of $Re_d = 22{,}000$ jet at two different stages of data processing. It shows that both velocity profiles agreed well. However, the Abel inversion before image pre-processing showed a slightly better agreement with PIV measurements.

Figure 9 compares the instantaneous and mean velocity fields of the helium jet of $Re_d = 11{,}000$ and $Re_d = 22{,}000$ obtained from PIV, schlieren with a horizontal knife-edge, schlieren with vertical knife-edge and shadowgraph, respectively. The sizes of the velocity vectors are proportional to their corresponding magnitudes, and the vectors are plotted on a velocity magnitude contour map. For every measurement technique, 500 image pairs had been used to calculate the mean flow field. Schlieren with horizontal knife-edge and shadowgraph showed excellent agreement with the PIV results. However, schlieren with vertical knife-edge failed to provide a meaningful velocity field. As mentioned earlier, the schlieren with vertical knife-edge detects only the horizontal components, $\partial n/\partial$r of the refractive index. This produced asymmetric illumination in the transverse direction of the jet. Due to asymmetric illumination, the "particle" size increases from the dark to the bright region in vertical knife-edge schlieren. The larger size "particles" incur bias error in the calculated velocity field. Even though several image filters were tested, they failed to restore any useable signals from vertical knife-edge schlieren images. A detailed analysis of the poor performance of vertical knife-edge schlieren is presented using the correlation plane statistics in subsequent sections.

For a better quantitative comparison, velocity magnitude iso-lines were plotted on the mean flow contour for $Re_d = 22{,}000$ as shown in Fig. 10. PIV, schlieren with horizontal knife-edge and shadowgraph all yielded comparable results. Time average jet centerline velocities at the nozzle exit were 611, 609, and 608 m/s for schlieren with a horizontal knife-edge, shadowgraph and PIV, respectively. The length of the potential core was approximately 3.7 cm for both PIV and horizontal knife-edge schlieren. Shadowgraph, however, showed a potential core length of 3 cm, shorter than PIV or schlieren. But all three measurement techniques agreed very well at the downstream of the jet.

The jet centerline velocity at the nozzle exit was 304 m/s (Mach = 0.3) and 611 m/s (Mach = 0.6), respectively, for $Re_d = 11{,}000$ and $Re_d = 22{,}000$. The mean axial velocity, U normalized by the centerline jet velocity, U_0 is plotted in Fig. 11a, b for both the Reynolds numbers. The near-field velocity profiles obtained from PIV, horizontal knife-edge schlieren, and shadowgraph were compared to flying, and stationary hot-wire measurements by Fellouah et al. (2009) for the Reynolds number ranging from 6000 to 30,000 on the near and intermediate region ($0 \leq x/d \leq 25$) of a round free jet. The comparison showed that the centerline velocity data of the turbulent helium jet obtained by horizontal knife-edge schlieren and shadowgraph agreed very well with the PIV measurements as well as with Fellouah et al. (2009). The axial jet velocity profiles appeared symmetric within experimental uncertainty. The jet tip velocity profile closely resembled the plug flow assumption. The velocity distribution retained a top-hat shape at 1.5–3d downstream of the nozzle exit for $Re_d = 11{,}000$ and $Re_d = 22{,}000$. The axial mean velocity profile at $x/d = 5$, $\mathrm{Re}_d = 11,000$ was not as developed as seen for $\mathrm{Re}_d = 22,000$, as it retained remnants of the initial conditions. This observation is consistent with the widely known fact that the length of the potential core decreases with increasing Reynolds number (Weisgraber and Liepmann 1998).

Figure 12 compares the mean centerline velocity decay of PIV and SIV techniques for $Re_d = 11{,}000$ and $Re_d = 22{,}000$. Schlieren with a horizontal knife-edge, shadowgraph agreed well with PIV. Figure 13a, b show the streamwise turbulence intensity, u'/U_0 at several axial locations for both the Reynolds numbers using various PIV and SIV techniques. Turbulence intensity was less inside the potential core and increased towards the jet boundary near the developing region. As the jet developed, the centerline turbulence intensity started growing. At any given axial location, the centerline turbulence intensity was lower for $Re_d = 22{,}000$ as compared to $Re_d = 11{,}000$. Reynolds shear stress, $< u'v' >$ is shown in Fig. 14, normalized by the square of the centerline velocity, U_0^2. The highest percentage of momentum exchange, which involves large-scale vortices, occurred in the jet shear layer. The location of maximum Reynolds stress got shifted away from the jet centerline with increased downstream distance. Reynolds stress calculated from SIV techniques agreed well with PIV measurements.

4.2 Correlation planes

Figure 15 shows the spatial correlations of the jet with $Re_d = 22{,}000$ obtained from PIV and SIV techniques at $x/d = 10$for three radial locations $r/d = 0,\ 0.5,\ 1$ and 1.5, respectively. It is evident from the Fig. 15 that PIV showed excellent spatial correlation at the near field region of the jet ($r/d = 0,\ 0.5$), but the spatial correlations became noisy at $r/d = 1$ and 1.5. For schlieren with horizontal knife-edge and shadowgraph, the spatial correlations showed similar behavior. These correlations appeared noisier than PIV. However, the presence of a single clear peak was prominent for all the radial locations. Spatial correlations from all the SIV techniques exhibited increasing noise in the correlation information at $r/d = 1$.

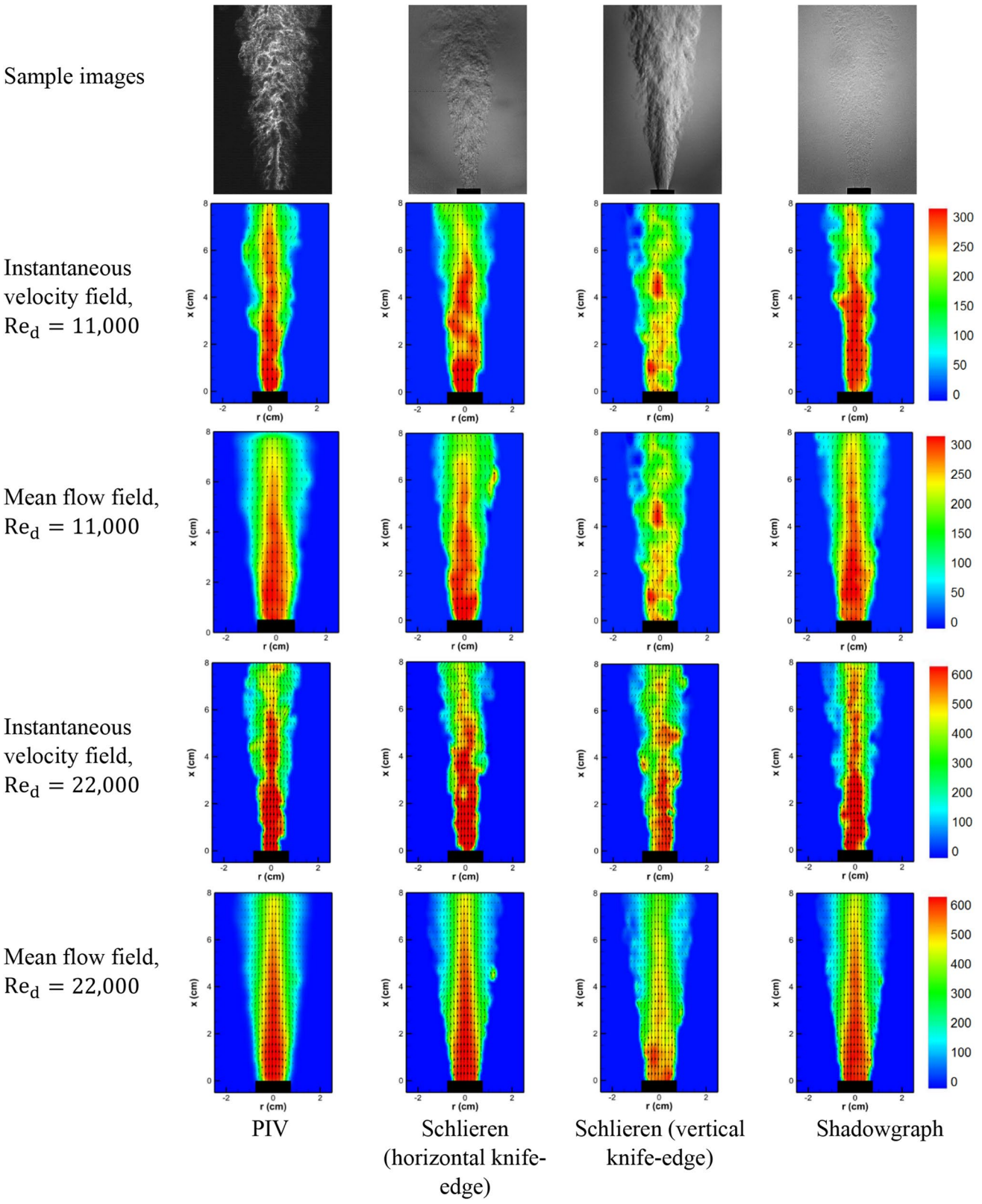

Fig. 9 Instantaneous and mean flow field colored by velocity magnitude from PIV, schlieren with horizontal knife-edge, schlieren with vertical knife-edge and shadowgraph for two different flow conditions, $Re_d = 11{,}000$ and $Re_d = 22{,}000$

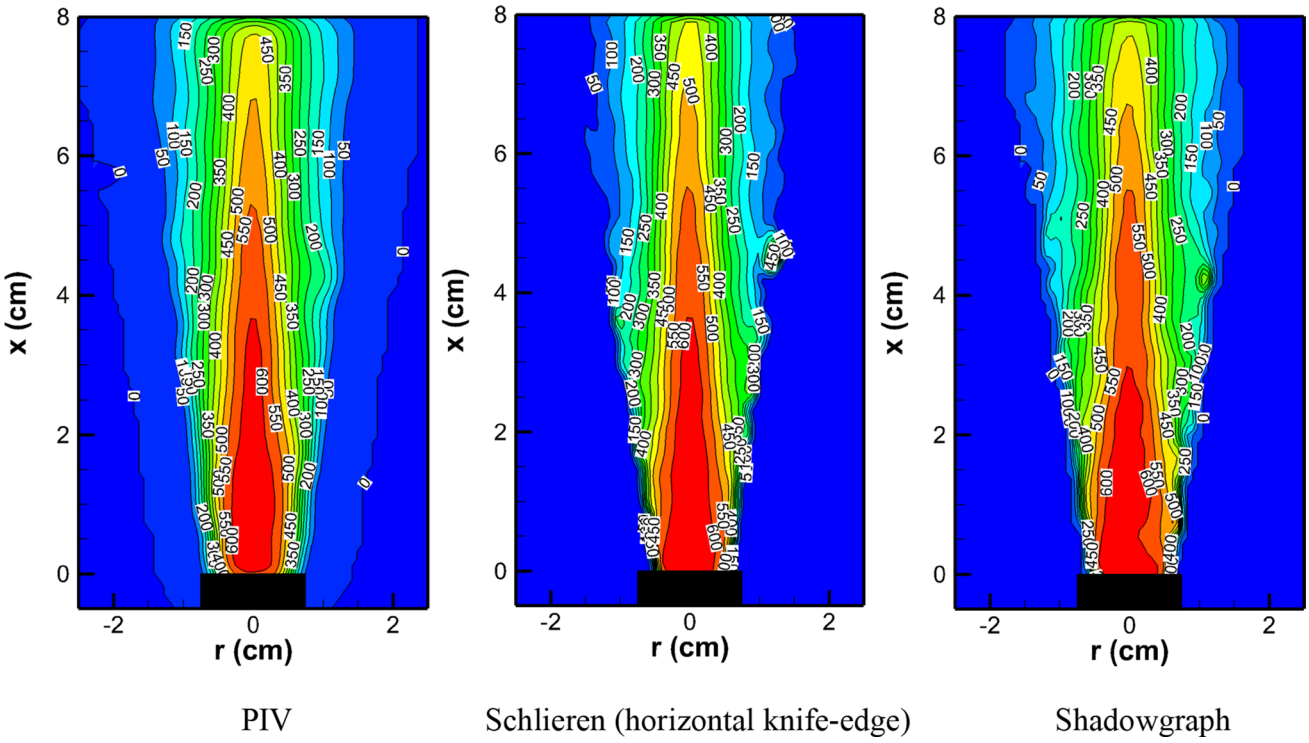

Fig. 10 Iso-lines of velocity magnitude on the mean flow field for $\mathrm{Re_d} = 22{,}000$

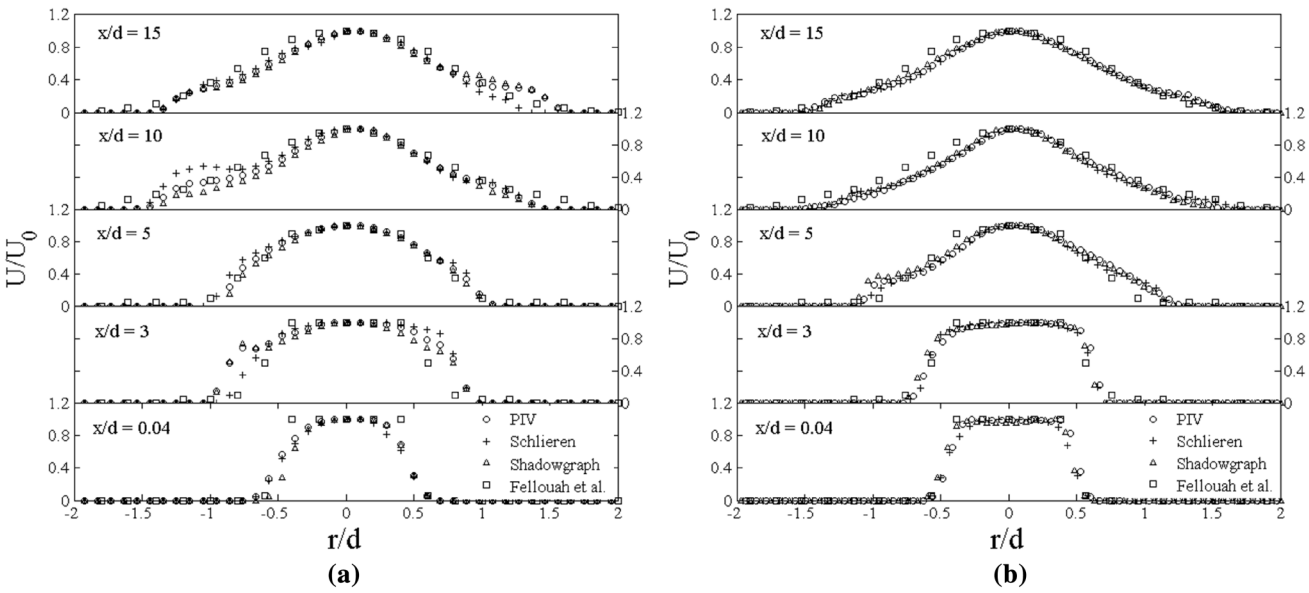

Fig. 11 Normalized streamwise mean velocity, U/U_0 at different axial positions for **a** $Re_d = 11{,}000$ and **b** $Re_d = 22{,}000$

This observation can be explained by looking at the turbulence intensity at $r/d = 1$.

Figure 16a plots the variation of the streamwise turbulence intensity, u'/U along the radial direction at $x/d = 10$, where u' is the streamwise velocity fluctuation and $\langle U \rangle$ is the mean velocity at that location. Since the contribution of the transverse turbulence intensity, $v'/\langle U \rangle$ to the overall turbulence intensity at any given location was an order of magnitude smaller (Bogey and Bailly 2006), only the effect of streamwise turbulence intensity was plotted and discussed here. In the developing region of the jet $x/d = 10$, the streamwise turbulence intensity maximized

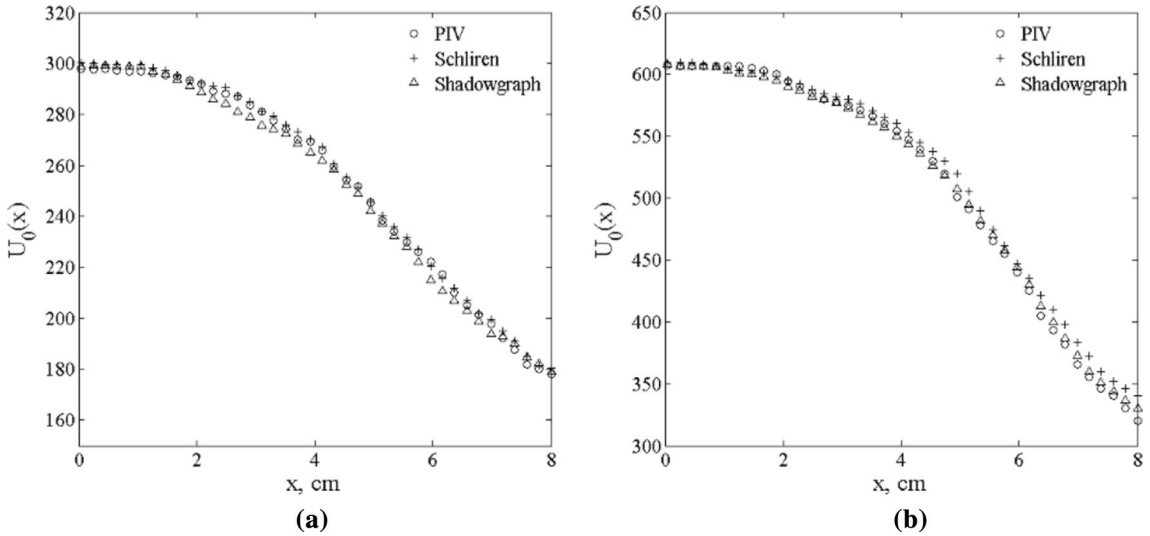

Fig. 12 Mean centerline velocity decay for **a** $Re_d = 11,000$ and **b** $Re_d = 22,000$

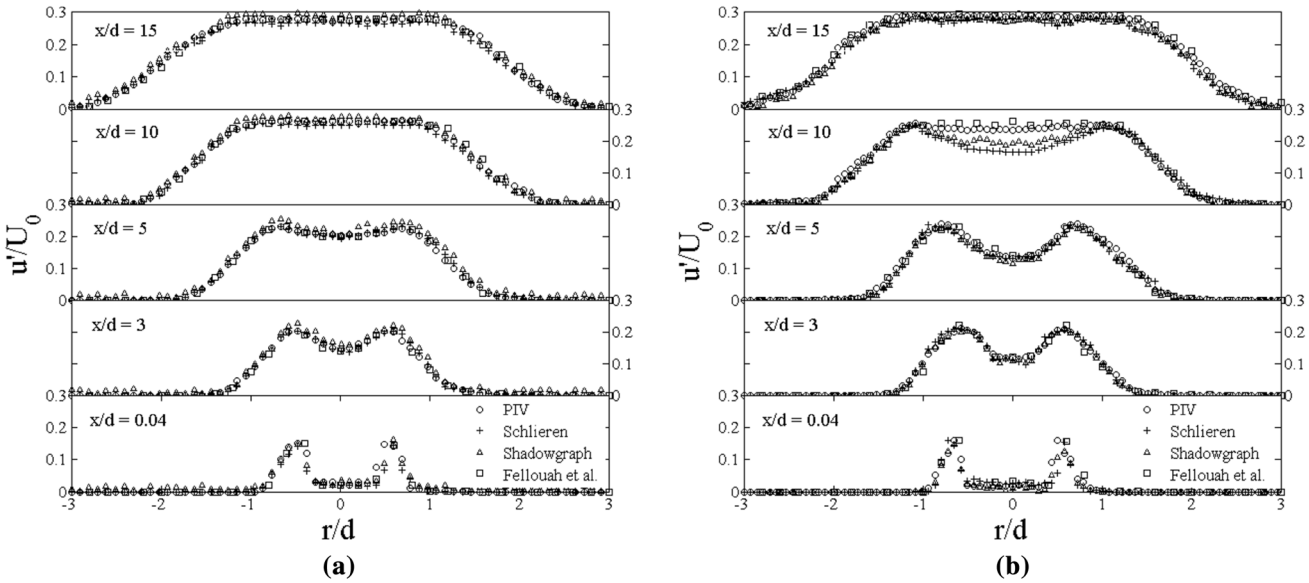

Fig. 13 Streamwise turbulence intensity, u'/U_0 at different axial locations for **a** $Re_d = 11,000$ and **b** $Re_d = 22,000$

within the region of $0.7 \leq r/d \leq 0.8$. Thus, the spatial correlations near $r/d = 1$ became noisy due to the presence of strong turbulence. Turbulence intensity dropped quickly after $r/d = 1.3$ and reached 10% of its maximum value at $r/d = 1.42$. However, this did not explain the correlation noises at $r/d = 1.5$. The noises at $r/d = 1.5$ were primarily due to lower seeding density. Perhaps a sophisticated scheme such as adaptive windowing and multi-frame was required to adapt this high gradient region to reduce noise. Bias error and RMS error increased with a lesser number of "particles." As the number of "particles" decreased towards the jet edge (or in the mixing layer), spatial correlations got noisy. This held true for both horizontal knife-edge schlieren and shadowgraph.

Figure 17 shows spatial correlations for the same experimental conditions and image velocimetry techniques at the jet centerline ($r/d = 0$) for four different streamwise locations, $x/d = 0.04$, 5, 10 and 20, respectively. Figure 17 exhibits the presence of clear, unambiguous peaks in the correlation planes near the jet centerline ($r/d = 0$) for PIV, horizontal knife-edge schlieren, and shadowgraph. Spatial correlations behaved in excellent fashion inside the potential core, $0.04 \leq x/d \leq 10$. However, SNR gradually went down for $x/d > 10$. This happened because as the

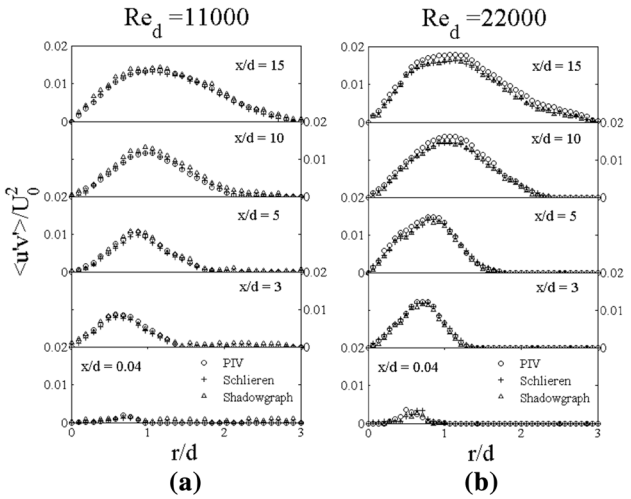

Fig. 14 Reynolds shear stress at different axial locations for **a** $Re_d = 11,000$ and **b** $Re_d = 22,000$

jet entered the developing region from the potential core, the streamwise turbulence intensity increased. Figure 16b shows the streamwise turbulence intensity variation along the jet centerline. The turbulence intensity increased nearly linearly with x/d. Turbulence intensity increased slowly between $0.04 \leq x/d \leq 10$, and it grew rapidly afterward. An increase in turbulence intensity for $x/d > 10$ induced noise in the spatial correlations.

As seen in the earlier sections, schlieren with vertical knife-edge failed to provide accurate velocity information. Correlation statistics discussed above could explain it from a statistical standpoint. Figures 15 and 17 show schlieren with vertical knife-edge had ambiguity in displacement correlation, the presence of multiple peaks of the same order, lower peak to peak ratio, higher background noise, and lower SNR.

4.3 Primary peak ratio (PPR), peak to correlation energy (PCE), and PDF of signal–noise

Cross-correlation SNR can be expressed as the ratio between the primary (the tallest) peak, $|\mathbb{C}_{\max}|$ and the second (next tallest) peak, $|\mathbb{C}_2|$ in the correlation plane. This can be written as:

$$\mathrm{PPR} = \frac{|\mathbb{C}_{\max}|}{|\mathbb{C}_2|} \tag{2}$$

This ratio is termed as the primary peak ratio (PPR) and is used as a measure of the detectability of the true

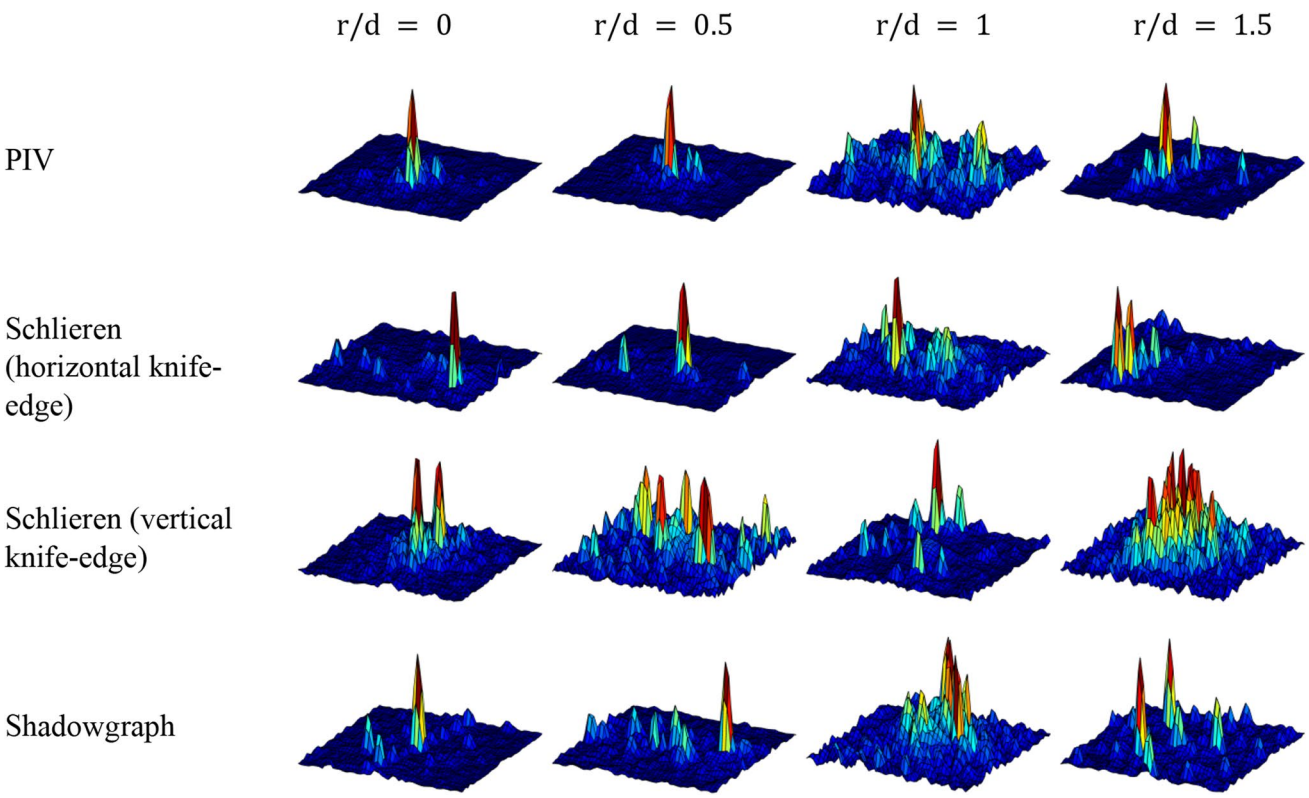

Fig. 15 Comparison of the spatial correlations of $Re_d = 22,000$ jet from PIV, schlieren with horizontal knife-edge, schlieren with vertical knife-edge and shadowgraph at $x/d = 10$ for various radial locations

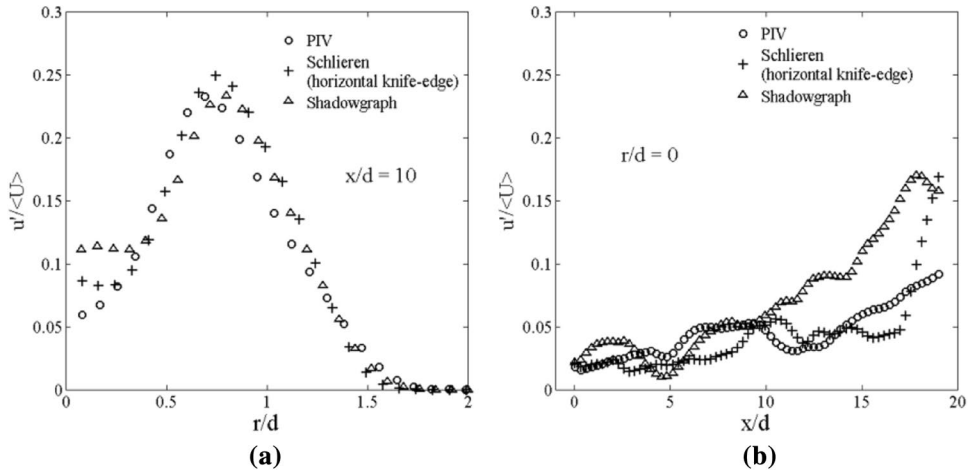

Fig. 16 Streamwise turbulence intensity, $u'/\langle U \rangle$ variation along **a** radial direction for $x/d = 10$ and **b** along axial direction for $r/d = 0$ of $Re_d = 22,000$ jet

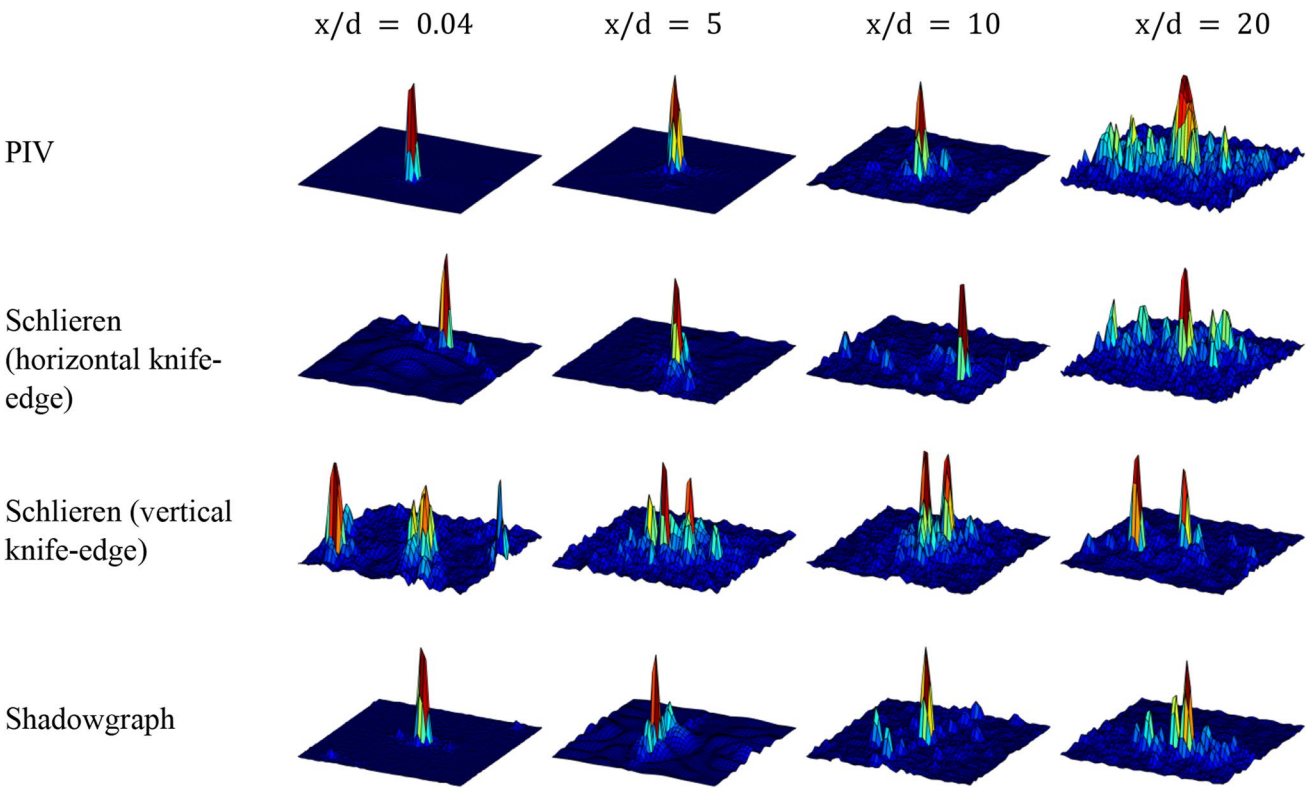

Fig. 17 Comparison of the spatial correlations of $Re_d = 22,000$ jet from PIV, schlieren with horizontal knife-edge, schlieren with vertical knife-edge and shadowgraph at jet centerline ($r/d = 0$) for various axial locations

displacement (Keane and Adrian 1990, 1991). Often a user-defined threshold (such as 1.2 or 1.3) for PPR is considered to validate the correlation. To remove the effect of any unwanted background noise in calculating PPR, the correlation planes were separated from the background noise. A typical cross-correlation plane separated from its background noise is represented in Fig. 18. The corresponding cross-correlation planes of the two image sets, with and without background noise, were subtracted one from the another to obtain the background noise. PPR for all image velocimetry techniques was compared along the radial direction at $x/d = 10$. PPR was found to be high, between 8.2 and 10.5 near the centerline at $r/d = 0$ for all measurement techniques except schlieren with a vertical knife-edge, as shown in Fig. 19a. Due to lower turbulent fluctuations at the jet centerline, spatial correlations detected unambiguous displacements of the turbulent structures or tracer "particles," hence PPR increased near the centerline. However,

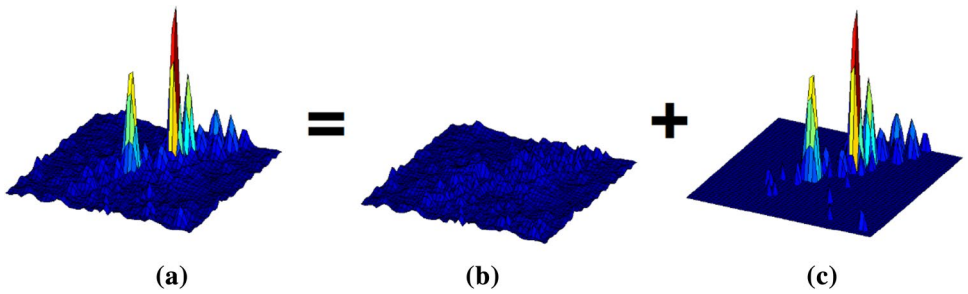

Fig. 18 Separation of cross-correlation plane from background noise. **a** Cross-correlation plane with background noise, **b** the correlation plane related to background noise, **c** cross-correlation plane without background noise

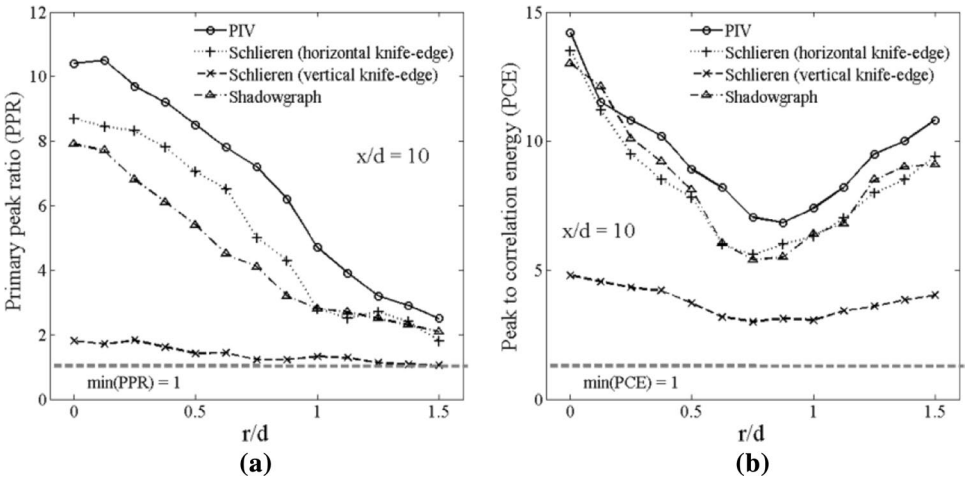

Fig. 19 Radial variation of **a** the primary peak ratio (PPR), the ratio between the primary correlation peak to the second tallest peak, **b** the peak to correlation energy (PCE) for PIV, schlieren with horizontal knife-edge, schlieren with vertical knife-edge and shadowgraph at $x/d = 10$ of $Re_d = 22,000$ jet

as we walked away from the centerline, PPR decreased almost linearly and reached a value of PPR ≈ 2 near the jet boundary, $r/d = 1.5$. This is in good agreement with Hain (Hain and Kähler 2007) who suggested that a threshold PPR, PPR ≥ 2 can reliably avoid the spurious vectors. Figure 19a shows that the highest PPR was found in PIV, although schlieren with horizontal knife-edge and shadowgraph showed good quality PPR as well. Another important observation was that PPR in shadowgraph was lower than horizontal knife-edge schlieren for $0 \leq r/d < 1$. These observations can be attributed to the fact that schlieren produced higher contrast images, which in turn helped to obtain best correlations. However, after $r/d \geq 1$ PPR for both these measurement techniques attained similar values.

PPR is an ad-hoc representation for SNR and the correlation plane statistics. It does not include information of the entire correlation plane. A better way to quantify the correlation SNR is to use the Peak signal to Correlation Energy (PCE) defined as the ratio between the magnitude of the cross-correlation plane and the correlation energy as,

$$\mathrm{PCE} = \frac{\left|\mathbb{C}_{\max}\right|^2}{E_c} \tag{3}$$

The magnitude of the correlation plane $\left|\mathbb{C}_{\max}\right|$ is the signal part representing the tallest peak in the correlation plane. Alternatively, the correlation energy which defines the noise part can be expressed as:

$$E_c = \int_{-\infty}^{\infty} \left|\mathbb{C}_{\max}\right|^2 \mathrm{d}x \tag{4}$$

However, the correlation plane has a finite size. Thus, the correlation energy of a finite size correlation plane can be calculated as:

$$E_c = \frac{1}{W}\left(\sum_{W} \left|\mathbb{C}_{\max}\right|^2\right) \tag{5}$$

where W is the size of the correlation plane. Figure 19b plots the radial variation of PCE for the similar settings as used to find PPR. PCE shows similar behavior for all measurement techniques except schlieren with a vertical knife-edge. PCE was found higher near the jet centerline and at the boundary/mixing layer but PCE reached a minimum for $0.6 < r/d < 1$. This occurred as the streamwise turbulence intensity affected PCE in a similar fashion as PPR, as shown in Fig. 16a. The streamwise turbulence intensity increased by 20–25% between $0.6 < r/d < 1$, which affected correlation plane statistics and in turn peak delectability.

To identify the correct velocity vector, the amplitude of the displacement correlation peak (signal) must

be larger than the amplitude of the tallest random peak (noise), SNR $\gg 1$. To evaluate the probability of SNR $\gg 1$, normalized probability density functions (PDF) of signal and noise peak amplitudes from the entire correlation plane are plotted in Fig. 20 for PIV and SIV techniques. The peak amplitude of the signal was much wider than the noise. Also, the mean signal peak amplitude shifted significantly for different measurement techniques. Both signal and noise peak amplitude PDFs for Schlieren with horizontal knife-edge and shadowgraph showed similar behavior. Signal peak amplitude shifting to far right for PIV indicated higher signal density compared to SIV techniques. Like the signal, noise peak amplitude also increased for PIV and shifted towards right and became wider, as compared to SIV techniques. However, this increase in noise level was insignificant relative to the increase in signal intensity for PIV. A lesser overlap between signal and noise peaks signified the better possibility of correlation (or in other words, increasing the probability for identification of the tallest displacement peak). An excess overlap of signal and noise peaks for schlieren with vertical knife-edge was responsible for producing spurious displacement peaks during spatial correlation as shown in Figs. 15 and 17.

5 Conclusions

This paper demonstrated a novel, inexpensive, easy to setup two-camera SIV technique that could resolve exceptionally high flow velocities. Statistical assessment of SIV techniques was performed for a high-velocity helium jet at two different Reynolds numbers, $Re_d = 11,000$, and $Re_d = 22,000$. The velocity field obtained by horizontal knife-edge schlieren with 40% cutoff and shadowgraph agreed well with the PIV results. Vertical knife-edge schlieren with 40% cutoff performed poorly due to inconsistent signal content.

Three filters were applied that improved the SNR of schlieren images, (a) a narrow-width, low-pass filter such as a uniform filter to remove high-frequency noise, (b) a nonlinear min/max filter to normalize the image contrast and (c) a Laplace filter to enhance and sharpen the turbulent structures. A "particle" image size, d_p between 2 and 3 pixels proved to work best.

The performance of the spatial correlations was quantitatively evaluated using PPR and PCE. A high value of PPR was observed near the jet centerline for schlieren with horizontal knife-edge and shadowgraph. PPR decreased linearly from jet centerline towards shear/mixing layer but

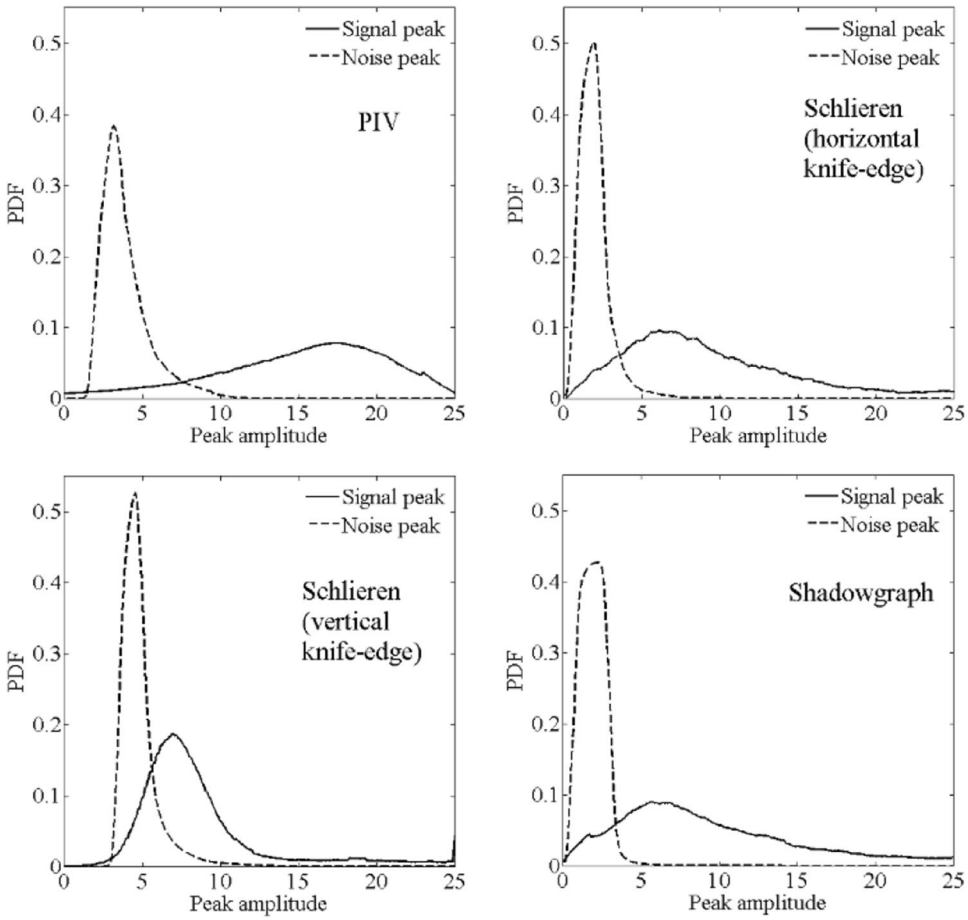

Fig. 20 The probability density functions (PDF) for the normalized amplitude of the displacement correlation peak (signal) and the tallest random correlation peak (noise) for PIV, schlieren with horizontal knife-edge, schlieren with vertical knife-edge and shadowgraph

retained PPR > 1. Due to higher turbulence intensity, the value of PCE dropped between $0.6 < r/d < 1$. PDF of signal and noise showed that PIV included higher noise than schlieren. However, the signal content in PIV was 2–3 folds higher than schlieren measurements.

SIV demonstrated promising results toward seedless velocity measurements, although it has some limitations. Due to the path integrated nature of current schlieren/shadowgraph techniques, it works best for axisymmetric or 2D flows but not for complex 3-D flows. It does not work for laminar flows because of the lack of turbulent structures. However, a focusing schlieren system can potentially be used to measure a three-dimensional flow field.

Acknowledgements The authors thank Dr. Jupyoung Kim of En'Urga Inc. for his help with the PIV experiment and Dr. Sayantan Bhattacharya of Mechanical Engineering, Purdue University for his guidance towards understanding the processing algorithms of Prana.

References

Abel NH (1826) Resolution d'un problem de mechanique. J Für Die Reine Angew Math 1:153–157

Arfken GB, Weber HJ, Harris FE (2012) Mathematical methods for physicists. Academic Press, 7th edition **(ISBN-13: 978-0123846549$4)**

Bogey C, Bailly C (2006) Large eddy simulations of transitional round jets: influence of the Reynolds number on flow development and energy dissipation. Phys Fluids 18(6):065101–65115. doi:10.1063/1.2204060

Canny J (1986) A computational approach to edge detection. IEEE Trans Pattern Anal Mach Intell 8(6):679–698. doi:10.1109/TPAMI.1986.4767851

Coppalle A, Joyeux D (1994) An optical technique for measuring mean and fluctuating values of particle concentrations in round jets. Exp Fluids 16(3):285–288

Eckstein A, Vlachos PP (2009) Digital particle image velocimetry (DPIV) robust phase correlation. Meas Sci Technol 20(5):055401–55402**(ISSN: 09570233)**

Elsinga GE, Oudheus den van BW, Scarano F, Watt DW (2003) Assessment and application of quantitative schlieren methods with bi-directional sensitivity: CCS and BOS. Proc. PSFVIP-4, p 1–17

Elsinga GE, Oudheus den van BW, Scarano F, Watt DW (2004) Assessment and application of quantitative schlieren methods: calibrated color schlieren and background oriented schlieren. Exp Fluids 36(2):309–325. doi:10.1007/s00348-003-0724-8

Fellouah H, Ball CG, Pollard A (2009) Reynolds number effects within the development region of a turbulent round free jet. Int J Heat Mass Transf 52(17/18):3943–3955. doi:10.1016/j.ijheatmasstransfer.2009.03.029

Fincham AM, Spedding GR (1997) Low cost, high resolution DPIV for measurement of turbulent fluid flow. Exp Fluids 23(6):449–462. doi:10.1007/s003480050135

Fu S, Wu Y (2001) Detection of velocity distribution of a flow field using sequences of Schlieren images. Opt Eng 40(8):1661–2001. doi:10.1117/1.1385337

Fu S, Wu Y, Kothari RD, Xing H (2000) Flow visualization using the negative-positive grid schlieren system and its image analysis. In: Carlomagno GM (eds) Proceedings of the ninth international symposium on flow visualization, I. Grant. Edinburgh, paper 324.

Garg S, Settles GS (1998) Measurements of a supersonic turbulent boundary layer by focusing schlieren deflectometry. Exp Fluids 25(3):254–264. doi:10.1007/s003480050228

Goldhahn E, Seume J (2007) The background oriented schlieren technique: Sensitivity, accuracy, resolution and application to a three-dimensional density field. Exp Fluids 43(2/3):241–250. doi:10.1007/s00348-007-0331-1

Hain R, Kähler CJ (2007) Fundamentals of multiframe particle image velocimetry (PIV). Exp Fluids 42(4):575–588. doi:10.1007/s00348-007-0266-6

Hargather MJ, Settles GS (2012) A comparison of three quantitative schlieren techniques. Opt Lasers Eng 50(1): 8–17. doi:10.1016/j.optlaseng.2011.05.012.

Hargather MJ, Lawson MJ, Settles GS, Weinstein LM (2011) Seedless velocimetry measurements by schlieren image velocimetry. AIAA J 49(3):611–620. doi:10.2514/1.J050753

Huang H, Dabiri D, Gharib M (1997) On errors of digital particle image velocimetry. Meas Sci Technol 8(12):1427–1440. doi:10.1088/0957-0233/8/12/007

http://sourceforge.net/projects/qi-tools/. Accessed 15 June 2015

Jonassen DR, Settles GS, Tronosky MD (2006) Schlieren "PIV" for turbulent flows. Opt Lasers Eng 44(3/4):190–208. doi:10.1016/j.optlaseng.2005.04.004

Joshi A, Schreiber W (2006) An experimental examination of an impulsively started incompressible turbulent jet. Exp Fluids 40(1):156–160

Keane RD, Adrian RJ (1990) Optimization of particle image velocimeters. I. Double pulsed systems. Meas Sci Technol 1(11):1202–1215. doi:10.1088/0957-0233/1/11/013

Keane RD, Adrian RJ (1991) Optimization of particle image velocimeters: II. multiple pulsed systems. Meas Sci Technol 2(10):963–974. doi:10.1088/0957-0233/2/10/013

Kegerise MA, Settles GS (2000) Schlieren image-correlation velocimetry and its application to free-convection flows. International Symposium on Flow Visualization, Edinburgh, paper 380, p 1–13.

Kindler K, Goldhahn E, Leopold F, Raffel M (2007) Recent developments in background oriented Schlieren methods for rotor blade tip vortex measurements. Exp Fluids 43(2/3):233–241. doi:10.1007/s00348-007-0328-9

Li L, Fu S, Witton JJ (2009) Schlieren methods for high pressure turbulent jet flames. J Energy Inst 82(2):114–118. doi:10.1179/174602209X427222

Marr D, Hildreth E (1980) Theory of edge detection. Proc R Soc Lond Ser B Biol Sci 207 (1167): 187–217. doi:10.1098/rspb.1980.0020

Mauger C, Méès L, Michard M, Lance M (2014) Velocity measurements based on shadowgraph-like image correlations in a cavitating micro-channel flow. Int J Multiphase Flow 58:301–313. doi:10.1016/j.ijmultiphaseflow.2013.10.004

Mayrhofer N, Woisetschläger J (2001) Frequency analysis of turbulent compressible flows by laser vibrometry. Exp Fluids 31(2):153–161

Papamoschou D (1989) A two-spark schlieren system for very-high velocity measurement. Exp Fluids 7(5):354–356. doi:10.1007/BF00198454

Pope SB (2000) Turbulent flows, 1st edn. Cambridge University Press, Cambridge **(ISBN-13: 978-0521598866$4)**

Raffel M (2015) Background-oriented schlieren (BOS) techniques. Exp Fluids 56:60. doi:10.1007/s00348-015-1927-5

Raffel M, Richard H, Meier GEA (2000a) On the applicability of background oriented optical tomography for large scale aerodynamic investigations. Exp Fluids 28(5):477–481. doi:10.1007/s003480050408

Raffel M, Tung C, Richard H, Yu Y, Meier GEA (2000b) Background oriented stereoscopic schlieren for full-scale helicopter vortex characterization. In: Carlomagno GM (ed) Proceedings of the ninth international symposium on flow visualization, I. Grant, Edinburgh

Rosenfeld A, Kak AC (1982) Digital picture processing, Morgan Kaufmann, Computer Science and Applied Mathematics series, 2nd edn **(ISBN-13: 978-0125973014$4)**

Scarano F, Benocci C, Riethmuller ML (1999) Pattern recognition analysis of the turbulent flow past a backward facing step. Phys Fluids 11(12):3808–3819

Settles GS (2001) Schlieren and shadowgraph techniques: visualizing phenomena in transparent media. Springer, Berlin

Watt DW, Donker Duyvis FJ, Van Oudeusden BW, Bannink WJ (2000) Calibrated schlieren and incomplete Abel inversion for the study of axisymmetric wind tunnel flows. In: Carlomagno GM (eds) Proceedings of the ninth international symposium on flow visualization, I. GrantI. Edinburgh, paper 363, 2000.

Weisgraber T, Liepmann D (1998) Turbulent structure during transition to self-similarity in a round jet. Exp Fluids 24(3):210–224. doi:10.1007/s003480050168

Westerweel J (1993) Digital particle image velocimetry—theory and application. Ph. D. Dissertation. Delft University Press, Delft

Yildirim B, Agrawal S (2005) Full-field measurements of self-excited oscillations in momentum-dominated helium jets. Exp Fluids 38(2):161–173

Zelenak M, Foldyna J, Scucka J, Hloch S, Riha Z (2015) Visualisation and measurement of high-speed pulsating and continuous water jets. Measurement 72: 1–9. doi:10.1016/j.measurement.2015.04.022